Numerical and analytical simulation of the growth of amyloid-β plaques

Andrey V. Kuznetsov

Department of Mechanical and Aerospace Engineering, North Carolina State University,

Raleigh, NC 27695-7910, USA; e-mail: avkuznet@ncsu.edu

Abstract

Numerical and analytical solutions to calculate the radius of an amyloid-β (Aβ) plaque over time were obtained. To my knowledge, this is the first model simulating the growth of Aβ plaques. It is shown that the plaque can reach the diameter of 50 μm after 20 years of growth only if degradation machinery responsible for degradation of Aβ monomers is malfunctioning. A mathematical model incorporates a nucleation and an autocatalytic growth using the Finke-Watzky model. The obtained system of ordinary differential equations was solved numerically, and for the simplified case of infinitely long Aβ monomer half-life, an analytical solution was found. Assuming that Aβ aggregates stick together, and using the distance between the plaques as an input parameter of the model, it was possible to calculate the plaque radius from the concentration of Aβ aggregates. This led to the formulation of the "cubic root hypothesis," which posits that Aβ plaque size increases as the cubic root of time. This hypothesis helps explain why larger plaques grow more slowly. Furthermore, the obtained results suggest that the plaque size is independent of the kinetic constants governing Aβ plaque agglomeration. This indicates that the kinetics of Aβ plaque agglomeration is not a limiting factor for the plaque growth. Instead, the plaque growth rate is limited by the rates of Aβ monomer production and degradation.

Keywords neuron; Alzheimer's disease; Finke−Watzky model, mathematical modeling; polymerization; cubic root hypothesis

Abbreviations

Aβ	amyloid-β
AD	Alzheimer's disease
APP	amyloid precursor protein
CV	control volume
F-W	Finke-Watzky

1. Introduction

Alzheimer's disease (AD) is a devastating neurodegenerative disorder, impacting nearly 50 million individuals globally. While there have been recent FDA-approved therapies that may decelerate its progression, there are currently no definitive cures for AD [1-5]. It is crucial to develop mechanistic models of processes involved in AD to pave the way for potential future treatments.

Senile plaques, primarily composed of accumulated amyloid-β (Aβ) peptide [6], represent a key characteristic of Alzheimer's disease (AD) [7]. A significant surge in interest surrounding Aβ aggregation stemmed from the amyloid cascade hypothesis, which posited that the formation of Aβ aggregates instigates all other pathological processes in AD. While this hypothesis has been extensively investigated, it has also faced recent criticism from some authors [8-11]. Whether senile plaques serve as a causative factor in AD or not remains a subject of ongoing investigation, but they undeniably stand as a distinctive hallmark of the disease [12-15].

Previous mechanistic models of AD [16-18] were primarily designed to elucidate intraneuronal mechanisms contributing to the development of AD. However, these investigations did not simulate the gradual extracellular buildup of Aβ plaques. The present study, on the other hand, aims to replicate the gradual growth of an Aβ plaque, a process that can span decades in humans. This process involves the generation of amyloid precursor protein (APP) within neurons and its subsequent cleavage by β- and γ-secretases at lipid membranes [6,14,19,20]. The majority of these newly formed Aβ monomers are released into the extracellular environment, where they hold the potential to aggregate [1].

2. Materials and models

2.1. Model equations

The F-W model simplifies the intricate process of protein aggregation into two key steps: nucleation and autocatalysis. During nucleation, new aggregates are continuously generated, whereas in the autocatalysis step, these aggregates experience rapid surface growth [21,22]. These two pseudoelementary reaction steps can be summarized as:

$$A \xrightarrow{k_1} B, \tag{1}$$

$$A + B \xrightarrow{k_2} 2B, \tag{2}$$

where A refers to a monomeric protein, and B represents a protein that has undergone amyloid conversion. The kinetic constants, denoted as k_1 and k_2, correspond to the rates of nucleation and autocatalytic

growth, respectively [21]. The primary nucleation process, as defined by Eq. (1), exclusively involves monomers. Conversely, secondary nucleation, described by Eq. (2), involves both monomers and preexisting aggregates of the same peptide (Eq. (2)) [23].

In [21], the Finke-Watzky (F-W) model was used to fit previously published data on Aβ aggregation [24,25]. Typically, this data are presented for two isoforms, Aβ40 and Aβ42, with the latter being more inclined to aggregate. In this context, the F-W model is applied to simulate the conversion of monomers, whose concentration is denoted as C_A, into aggregates, whose concentration is denoted as C_B. These aggregates encompass various forms of Aβ oligomers, protofibrils, and fibrils [7]. Aβ aggregates formed by this process assemble in amyloid plaques. It is worth noting that the simplified nature of the F-W model does not allow for differentiation between various aggregate types and sizes.

If soluble Aβ were to diffuse at a slower rate than the pace of aggregation, it would lead to growth primarily occurring at the tips of aggregates, resulting in a branching, tree-like structure. However, this contradicts what has been observed in experiments [26]. The rapid diffusion of Aβ monomers suggests minimal variation in their concentration, C_A, within the interneuronal space. With this assumption, the control volume (CV) displayed in Fig. 1 can be treated as a lumped capacitance body. Expressing the conservation of Aβ monomers within this CV yields the following equation:

$$\frac{dC_A}{dt} = -k_1 C_A - k_2 C_A C_B - C_A \frac{\ln(2)}{T_{1/2,A}} + \frac{q_{A,0}}{L}. \tag{3}$$

The first term on the right-hand side of Eq. (3) simulates the rate of conversion of Aβ monomers into aggregates, while the second term simulates the rate of this conversion through autocatalytic growth. These expressions for the first and second terms come from applying the law of mass action to the reactions described by Eqs. (1) and (2), respectively. The third term on the right-hand side of Eq. (3) accounts for the rate at which Aβ monomers degrade. The fourth term denotes the rate of Aβ monomer production, as Aβ monomers are continually generated through the cleavage of APP [27,28].

If the conservation of Aβ aggregates is written for the CV, the following equation is obtained:

$$\frac{dC_B}{dt} = k_1 C_A + k_2 C_A C_B. \tag{4}$$

The first term on the right-hand side of Eq. (4) simulates the rate at which Aβ aggregates are produced through nucleation, while the second term simulates the rate of their production via autocatalytic growth. These terms have equal magnitudes but opposite signs compared to the first and second terms in Eq. (3).

This is because, in the F-W model, the rate of aggregate production equals the rate of monomer disappearance. Eqs. (3) and (4) only account for the finite half-life of Aβ monomers, as it is expected that the half-life of Aβ aggregates is significantly longer [29].

The initial conditions are as follows:

At $t=0$: $C_A=0$, $C_B=0$. (5a,b)

The sole independent variable in the model is time, *t*. The dependent variables are listed in Table 1, while the parameters employed in the model are listed in Table 2.

Table 1. Dependent variables utilized in the model.

Symbol	Definition	Units
C_A	Concentration of Aβ monomers	μM
C_B	Concentration of Aβ aggregates	μM
r_{ABP}	Radius of a growing Aβ plaque	μm

Table 2. Model parameters and their estimated values.

Symbol	Definition	Units	Value or range	Reference or estimation method	Value(s) used in computations
k_1	Rate constant for the first pseudoelementary step of the F-W model, describing the nucleation of Aβ aggregates	s^{-1}	2.22×10^{-9} [a]	[21,24]	2.22×10^{-9}
k_2	Rate constant for the second pseudoelementary step of the F-W	$\mu M^{-1}\ s^{-1}$	9.44×10^{-6} [a]	[21,24]	9.44×10^{-6}

	model, describing the autocatalytic growth of Aβ aggregates				
L	Half distance between senile plaques	μm	50	Estimated from Fig. 1a in [30]	50
N_A	Avogadro's number	mol^{-1}	6.022×10^{23}		6.022×10^{23}
$q_{A,0}$	Rate of production of Aβ monomers per unit area of one of the CV's faces. Aβ production is a surface phenomenon, occurring at the lipid membrane. The model assumes that all Aβ is released from one face of the CV. Aβ production is calculated per unit area of that face. The rate of Aβ production per unit volume then is $q_{A,0}/L$.	μM μm s^{-1}	1.1×10^{-5} [b]	[31]	1.1×10^{-5}
$T_{1/2,A}$	Half-life of Aβ monomers	s	4.61×10^{3} [c]	[32]	4.61×10^{3}, 4.61×10^{9} (to represent $T_{1/2,A}\to\infty$)
$V_{FB,av}$	Average volume of an Aβ fibril	μm^3	1.06×10^{-6} [d]	[33]	1.06×10^{-6}

	composing an Aβ plaque				

[a] Values reported in [21] were obtained by curve-fitting data from [24]. $k_1 = 8\times10^{-6}$ h^{-1}, $k_2 = 3.4\times10^{-2}$ μM^{-1} h^{-1} [21].

[b] According to [31], the human brain produces Aβ42 monomers at a rate of 0.33×10^{-6} μmol s^{-1}. Considering the approximate volume of the brain as 1.5×10^{15} μm^3, the rate of Aβ42 production per unit volume is estimated to be 2.2×10^{-22} μmol μm^{-3} s^{-1}. In a small cube with a side length of L (representing the CV in Fig. 1), the rate of Aβ42 production is 2.75×10^{-17} μmol s^{-1}. Production of Aβ monomers occurs at the lipid membrane [34]. For this reason, the production rate of Aβ42 was normalized assuming that all of it is produced at one face of the CV with the area of L^2, and the rate of Aβ42 production per unit area of that face was calculated. The obtained value of $q_{A,0}$ is 1.1×10^{-20} μmol μm^{-2} s^{-1} $=1.1\times10^{-5}$ μM μm s^{-1}. The rate of Aβ42 production per unit volume of the CV can then be calculated as $q_{A,0}/L$.

[c] According to [32], the value is 1.28 hours.

[d] Aβ protofibrils have a length between 60 to 220 nm (and thus an average length of 140 nm) and a diameter 3.1 of nm [33]. This gives an average volume of a protofibril of $V_{FB,av} = 1.06\times10^{-6}$ μm^3.

The dimensionless form of Eqs. (3) and (4) can be expressed as follows:

$$\frac{dC_A^*}{dt^*} = -C_A^* - C_A^* C_B^* - C_A^* \frac{\ln(2)}{T_{1/2,A}^*} + q_{A,0}^* , \tag{6}$$

$$\frac{dC_B^*}{dt^*} = C_A^* + C_A^* C_B^* . \tag{7}$$

The dimensionless form of the initial conditions defined by Eq. (5) is as follows:

At $t^* = 0$: $C_A^* = 0$, $C_B^* = 0$. (8a,b)

Table 3 presents the dimensionless independent variable, while Table 4 summarizes the dimensionless dependent variables. Table 5 provides the dimensionless parameters used in the model.

Eqs. (6) and (7) constitute a pair of ordinary differential equations. MATLAB's ODE45 solver (MATLAB R2020b, MathWorks, Natick, MA, USA) was employed to solve these equations subject to initial conditions given by Eq. (8). To ensure accuracy of the solution, the error tolerance parameters, RelTol and AbsTol, were set to 1e-10.

Table 3. Dimensionless independent variable in the model.

Symbol	Definition
t^*	$t k_1$

Table 4. Dimensionless dependent variables employed in the model.

Symbol	Definition
C_A^*	$C_A k_2 / k_1$
C_B^*	$C_B k_2 / k_1$
r_{ABP}^*	r_{ABP} / L

Table 5. Dimensionless parameters utilized in the model.

Symbol	Definition	Value obtained using the dimensional parameter values listed in the last column of Table 2
N_A^*	$\frac{N_A}{a_{21}} L^3 \frac{k_1}{k_2}$	1.77×10^4
$q_{A,0}^*$	$q_{A,0} k_2 / \left(k_1^2 L\right)$	4.21×10^5
$T_{1/2,A}^*$	$T_{1/2,A} k_1$	1.02×10^1, 1.02×10^{-5} (to represent $T_{1/2,A}^* \to \infty$)

$V^*_{FB,av}$	$V_{FB,av} / L^3$	8.45×10^{-12}

When Eqs. (6) and (7) were added together, the following result was obtained:

$$\frac{dC^*_A}{dt^*}+\frac{dC^*_B}{dt^*}=-C^*_A\frac{\ln(2)}{T^*_{1/2,A}}+q^*_{A,0}\,. \tag{9}$$

By integrating Eq. (9) with respect to time under the condition of $T_{1/2,A}\to\infty$ and using the initial condition given by Eq. (8), the following result was obtained:

$$C^*_A+C^*_B=q^*_{A,0}t^*\,. \tag{10}$$

The increase in $C^*_A+C^*_B$ over time is attributed to the continuous generation of Aβ monomers.

By eliminating C^*_A from Eq. (6) using Eq. (10), the following was obtained:

$$\frac{dC^*_B}{dt^*}=q^*_{A,0}t^*-C^*_B+\left(q^*_{A,0}t^*-C^*_B\right)C^*_B\,. \tag{11}$$

Eq. (11) is similar to the one examined in [35]. To find the exact solution of Eq. (12) with the initial condition given by Eq. (8b), the DSolve function followed by the FullSimplify function in Mathematica 13.3 (Wolfram Research, Champaign, IL) is utilized. The resulting solution is presented below:

$$C^*_B\left(t^*\right)=-1+\frac{\exp\left(t^*+q^*_{A,0}\frac{\left(t^*\right)^2}{2}\right)\sqrt{q^*_{A,0}}}{\sqrt{q^*_{A,0}}-\sqrt{2}F\left(\frac{1}{\sqrt{2q^*_{A,0}}}\right)+\sqrt{2}\exp\left(t^*+q^*_{A,0}\frac{\left(t^*\right)^2}{2}\right)F\left(\frac{1+q^*_{A,0}t^*}{\sqrt{2q^*_{A,0}}}\right)}\,. \tag{12}$$

In this equation, $F(x)$ represents Dawson's integral:

$$F(x)=\frac{1}{2}\sqrt{\pi}\,e^{-x^2}\,erfi(x)\,, \tag{13}$$

where $erfi(x)$ is the imaginary error function.

C^*_A can then be determined using Eq. (10) as:

$$C_A^* = q_{A,0}^* t^* - C_B^* . \tag{14}$$

The exact solution given by Eqs. (12) and (14) is quite complex. A more elegant approximate solution, which is also valid when $T_{1/2,A} \to \infty$, is as follows:

$$C_A^* = \frac{q_{A,0}^*}{1 + q_{A,0}^* t^*} , \tag{15}$$

$$C_B^* = q_{A,0}^* t^* . \tag{16}$$

As $t^* \to \infty$, Eq. (15) predicts that $C_A^* \to 0$. It is important to note that Eqs. (15) and (16) are useful for large times. However, they are not applicable when $t^* \to 0$; for instance, Eq. (15) yields $C_A^*(0) = q_{A,0}^*$, which contradicts the initial condition specified in Eq. (8a).

The growth of the core of an Aβ plaque (Fig. 1) can be simulated as follows. The volume of the core can be determined as:

$$V_{ABP} = \frac{C_B}{a_{21}} N_A L^3 V_{FB,av} = \frac{4}{3}\pi r_{ABP}^3 , \tag{17}$$

where $a_{21} = 10^{21} \frac{\mu\text{M}\ \mu\text{m}^3}{\text{mol}}$ represents the conversion factor from $\frac{\text{mol}}{\mu\text{m}^3}$ to μM, and $V_{FB,av}$ denotes the average volume of an Aβ aggregate structure, such as a fibril, forming the core of an Aβ plaque.

When expressed with dimensionless parameters, Eq. (17) can be reformulated as:

$$C_B^* N_A^* V_{FB,av}^* = \frac{4}{3}\pi \left(r_{ABP}^* \right)^3 . \tag{18}$$

By solving Eq. (18) for r_{ABP}, the following result was obtained:

$$r_{ABP}^*\left(t^*\right) = \left(\frac{3}{4\pi} C_B^*\left(t^*\right) N_A^* V_{FB,av}^* \right)^{1/3} . \tag{19}$$

By substituting Eq. (16) into Eq. (19), the following approximate solution for the radius of the Aβ plaque was obtained:

$$r_{ABP}^*\left(t^*\right) = \left(\frac{3}{4\pi} q_{A,0}^* N_A^* V_{FB,av}^* t^* \right)^{1/3} . \tag{20}$$

Reverting to dimensional coordinates, the following result was obtained:

$$r_{ABP}(t) = \left(\frac{3}{4\pi} \frac{N_A q_{A,0} L^2}{a_{21}} V_{FB,av} t \right)^{1/3}. \tag{21}$$

Eq. (21) suggests that the size of Aβ plaques increases proportionally to the cubic root of time. Intriguingly, Eq. (21) also predicts that the radius of an Aβ plaque remains independent of the kinetic constants that describe the rate of Aβ plaque agglomeration, k_1 and k_2. This observation is in line with findings from [36], which revealed that individual plaques can form relatively quickly, typically within approximately 24 hours. Hence, the kinetics of Aβ plaque agglomeration does not appear to be a limiting factor. Instead, the growth of these plaques is constrained by the rate of Aβ monomer production and the rate at which these monomers degrade.

Based on Eq. (21), one can deduce that the rate of Aβ plaque growth is

$$\frac{dr_{ABP}}{dt} = \frac{1}{6^{2/3}\pi^{1/3}} \left(\frac{N_A q_{A,0} L^2}{a_{21}} V_{FB,av} \right)^{1/3} t^{-2/3}. \tag{22}$$

Eq. (22) provides an explanation for why the growth of Aβ plaques decelerates over time. This means that smaller plaques tend to experience faster growth compared to larger plaques, a phenomenon observed in previous research [37].

2.2. Sensitivity analysis

The sensitivity of the radius of a growing Aβ plaque, r_{ABP}, to the three parameters in Eq. (21), L, $q_{A,0}$, and $V_{FB,av}$, was investigated. To do this, the local sensitivity coefficients [38-41] were computed. The sensitivity coefficients represent the first-order partial derivatives of the observable (in this case, the radius of the growing Aβ plaque) to L, $q_{A,0}$, and $V_{FB,av}$, for example, $\frac{\partial r_{ABP}}{\partial L}$. The dimensionless relative sensitivity coefficients [39,42] were then determined using the following formula, for example:

$$S_L^{r_{ABP}} = \frac{L}{r_{ABP}} \frac{\partial r_{ABP}}{\partial L}. \tag{23}$$

Utilizing Eq. (21):

$$S_L^{r_{ABP}} = \frac{2}{3}, \tag{24}$$

$$S_{q_{A,0}}^{r_{ABP}} = \frac{1}{3}, \tag{25}$$

$$S_{V_{FB,av}}^{r_{ABP}} = \frac{1}{3}. \tag{26}$$

The positive values of $S_L^{r_{ABP}}$, $S_{q_{A,0}}^{r_{ABP}}$, and $S_{V_{FB,av}}^{r_{ABP}}$ indicate that an increase in L, $q_{A,0}$, and $V_{FB,av}$ will result in an increase in r_{ABP}.

3. Results

Figs. 2-5 were generated using the parameter values listed in Table 2, unless otherwise specified.

In the scenario where Aβ monomers have an infinite half-life, the concentration of Aβ aggregates, C_B, increases linearly with time, consistent with the approximate solution provided by Eq. (16) (Fig. 2a). However, it is worth noting that this approximate solution is not valid at small times within the range of [0 0.1 year] (Fig. 2b). In the case where the machinery responsible for degrading Aβ monomers functions normally ($T_{1/2,A} = 4.61 \times 10^3$ s), the computational result indicates a significantly lower concentration of aggregates (Fig. 2a). This suggests that the formation of Aβ plaques is only possible when the proteolytic machinery responsible for Aβ monomer degradation [43] malfunctions.

In the scenario where Aβ monomers have an infinite half-life, the concentration of Aβ monomers, C_A, decreases as time progresses (Fig. 3a,b). This decline is a consequence of the increasing concentration of Aβ aggregates (Fig. 2a), leading to faster autocatalytic conversion of monomers into aggregates as described by Eq. (4). Notably, the approximate solution provided by Eq. (15) closely agrees with the numerical solution (Fig. 3a,b). On the other hand, when the machinery responsible for Aβ monomer degradation functions normally ($T_{1/2,A} = 4.61 \times 10^3$ s), the computational results predict a consistently low and uniform level of Aβ monomers, at any time (Fig. 3a,b).

In the scenario of infinite half-life for Aβ monomers, the radius of a growing Aβ plaque, r_{ABP}, increases in proportion to the cubic root of time, $t^{1/3}$, in agreement with the approximate solution provided in Eq. (21) (Fig. 4a). The agreement between the approximate and numerical solutions is excellent, except for when *t* is within the small time range of [0 0.1 year] (Fig. 4b). However, if the machinery responsible for

Aβ monomer degradation functions normally ($T_{1/2,A} = 4.61\times10^3$ s), the computational result predicts a much slower increase rate for the radius of an Aβ plaque over time (Fig. 4a). This suggests that the cubic root hypothesis is applicable only when at least 0.1 year has passed since the beginning of Aβ aggregation, and the Aβ monomer degradation mechanism is not functioning correctly.

Fig. 5a illustrates the relationship between the radius of Aβ plaques after 20 years of growth and the half-distance between these plaques, *L*. When $T_{1/2,A} \to \infty$, r_{ABP} increases with *L*. This occurs because, for a uniform volumetric production rate of Aβ monomers, a smaller number of plaques (larger distances between them) allows each individual plaque to access a greater supply of Aβ, thus enabling it to grow to a larger size. If $L = 150$ μm, the plaque's diameter after 20 years of growth is approximately 50 μm, which agrees with the representative diameter of an Aβ plaque observed in [30]. In the case of infinite half-life for Aβ monomers, the approximate solution provided by Eq. (21) precisely matches the numerical solution (Fig. 5a). However, if the machinery responsible for Aβ monomer degradation is functioning normally ($T_{1/2,A} = 4.61\times10^3$ s), somewhat counterintuitively, an increase in *L* results in a slight reduction of r_{ABP} (Fig. 5a). This outcome stems from the fact that Aβ monomer degradation occurs volumetrically (as described in Eq. (3)), and a larger control volume (indicated by a larger *L*) implies less available Aβ for plaque growth.

Fig. 5b illustrates how the radius of Aβ plaques after 20 years of growth is influenced by the rate of Aβ monomer production. When $T_{1/2,A} \to \infty$, r_{ABP} is directly proportional to $q_{A,0}^{1/3}$ because a higher production rate of Aβ monomers results in a greater supply of Aβ available for plaque growth (Fig. 5b). If $q_{A,0} = 10^{-4}$ μM μm s^{-1}, the diameter of the Aβ plaque after 20 years of growth is approximately 50 μm, the value reported in [30]. In the scenario where Aβ monomers have an infinite half-life, the approximate solution given by Eq. (21) precisely agrees with the numerical solution (Fig. 5b). However, if the machinery responsible for Aβ monomer degradation is functioning normally ($T_{1/2,A} = 4.61\times10^3$ s), the plaque grows nearly at the same rate as it does for $T_{1/2,A} \to \infty$. This is because Aβ monomer production is continuous, and the monomers convert into Aβ plaques before they can be broken down.

Fig. 5c demonstrates the relationship between the radius of Aβ plaques after 20 years of growth and the average volume of Aβ fibrils that compose the plaque. The F-W model predicts aggregate concentration, not their size. Consequently, aggregate size, represented by its volume, $V_{FB,av}$, is an independent parameter in the proposed model. With larger aggregate sizes, Aβ plaques, composed of larger particles,

grow to a greater size. If $T_{1/2,A} \to \infty$ and $V_{FB,av} = 10^{-5}$ μm^3, the diameter of the Aβ plaque after 20 years of growth approximately equals 50 μm, as observed in [30]. In the case of an infinite half-life of Aβ monomers, the approximate solution provided by Eq. (21) agrees perfectly with the numerical solution (Fig. 5c). However, if the machinery responsible for Aβ monomer degradation is functioning normally ($T_{1/2,A} = 4.61 \times 10^3$ s), Aβ plaques grow to a smaller size compared to the scenario of $T_{1/2,A} \to \infty$ (Fig. 5c).

4. Discussion, model limitations, and future directions

The analytical solution predicting the radius of Aβ plaques over time suggests that these plaques increase in size following a cubic root relationship with time. This result helps in clarifying the reason why larger plaques exhibit slower growth. Moreover, the model indicates that the radius of Aβ plaques remains unaffected by variations in the kinetic constants governing Aβ plaques' aggregation rate, k_1 and k_2. This observation implies that the kinetics of Aβ aggregation is not the primary limiting factor dictating Aβ plaque growth; rather, the rates of Aβ monomer production and degradation play more crucial roles.

There are a number of limitations associated with this model. One limitation is the use of the lumped capacitance model to simulate the buildup of Aβ monomer and aggregate concentrations. This model assumes that these concentrations vary with time but not with location within the CV. Given that Aβ monomers are generated at lipid membranes, it is reasonable to expect concentration variations between neurons, with the highest concentration occurring at the lipid membrane. Future models should consider incorporating diffusion-driven transport of Aβ monomers within the interneuronal space, as explored in a preliminary manner in [44]. Another limitation arises from the utilization of the F-W model for Aβ aggregation, which does not distinguish between aggregates of varying sizes, such as dimers, oligomers, protofibrils, and fibrils [6]. Addressing this limitation in future research by employing more precise protein polymerization models will lead to more accurate characterization of the structure of Aβ plaques, in particular, of their heterogeneity.

Data accessibility. This article has no additional data.

Authors' contributions. AVK is the sole author of this paper.

Competing interests. The author declares no competing interests.

Funding statement. AVK acknowledges the support provided by the National Science Foundation (grant CBET-2042834) and the Alexander von Humboldt Foundation through the Humboldt Research Award.

References

1. Rahman MM, Lendel C. 2021 Extracellular protein components of amyloid plaques and their roles in Alzheimer's disease pathology. *Molecular Neurodegeneration* **16,** 59. (doi:10.1186/s13024-021-00465-0)

2. Cummings J, Zhou Y, Lee G, Zhong K, Fonseca J, Cheng F. 2023 Alzheimer's disease drug development pipeline: 2023. *Alzheimer's Dement.* **9,** e12385. (doi:10.1002/trc2.12385)

3. Hardy J. 2006 A hundred years of Alzheimer's disease research. *Neuron* **52,** 3-13. (doi:10.1016/j.neuron.2006.09.016)

4. Maqbool M, Mobashir M, Hoda N. 2016 Pivotal role of glycogen synthase kinase-3: A therapeutic target for Alzheimer's disease. *Eur. J. Med. Chem.* **107,** 63-81. (doi:10.1016/j.ejmech.2015.10.018)

5. Hung S, Fu W. 2017 Drug candidates in clinical trials for Alzheimer's disease. *J. Biomed. Sci.* **24,** 47. (doi:10.1186/s12929-017-0355-7)

6. Hampel H, Hardy J, Blennow K, Chen C, Perry G, Kim SH, Villemagne VL, Aisen P, Vendruscolo M, Iwatsubo T, Masters CL, Cho M, Lannfelt L, Cummings JL, Vergallo A. 2021 The amyloid-β pathway in Alzheimer's disease. *Mol. Psychiatry* **26,** 5481-5503. (doi:10.1038/s41380-021-01249-0)

7. Chen G, Xu T, Yan Y, Zhou Y, Jiang Y, Melcher K, Xu HE. 2017 Amyloid beta: Structure, biology and structure-based therapeutic development. *Acta Pharmacol. Sin.* **38,** 1205-1235. (doi:10.1038/aps.2017.28)

8. Hardy JA, Higgins GA. 1992 Alzheimers-disease - the amyloid cascade hypothesis. *Science* **256,** 184-185. (doi:10.1126/science.1566067)

9. Karran E, Mercken M, De Strooper B. 2011 The amyloid cascade hypothesis for Alzheimer's disease: An appraisal for the development of therapeutics. *Nature Reviews Drug Discovery* **10,** 698-712. (doi:10.1038/nrd3505)

10. Herrup K. 2015 The case for rejecting the amyloid cascade hypothesis. *Nat. Neurosci.* **18,** 794-799. (doi:10.1038/nn.4017)

11. Ricciarelli R, Fedele E. 2017 The amyloid cascade hypothesis in Alzheimer's disease: It's time to change our mind. *Curr. Neuropharmacol.* **15,** 926-935. (doi:10.2174/1570159X15666170116143743)

12. Murphy MP, LeVine H3. 2010 Alzheimer's disease and the amyloid-beta peptide. *J. Alzheimers Dis.* **19,** 311-323. (doi:10.3233/JAD-2010-1221)

13. Hardy J, Selkoe DJ. 2002 The amyloid hypothesis of Alzheimer's disease: Progress and problems on the road to therapeutics. *Science* **297,** 353-356. (doi:10.1126/science.1072994)

14. O'Brien RJ, Wong PC. 2011 Amyloid precursor protein processing and Alzheimer's disease. *Annual Review of Neuroscience, Vol 34* **34,** 185-204. (doi:10.1146/annurev-neuro-061010-113613)

15. Selkoe DJ, Hardy J. 2016 The amyloid hypothesis of Alzheimer's disease at 25years. *Embo Molecular Medicine* **8,** 595-608. (doi:10.15252/emmm.201606210)

16. Kuznetsov IA, Kuznetsov AV. 2018 How the formation of amyloid plaques and neurofibrillary tangles may be related – A mathematical modelling study. *Proceedings of the Royal Society A* **474,** 20170777. (doi:10.1098/rspa.2017.0777)

17. Kuznetsov IA, Kuznetsov AV. 2018 Simulating the effect of formation of amyloid plaques on aggregation of tau protein. *Proceedings of the Royal Society A-Mathematical Physical and Engineering Sciences* **474,** 20180511. (doi:10.1098/rspa.2018.0511)

18. Torok J, Maia PD, Verma P, Mezias C, Raj A. 2021 Emergence of directional bias in tau deposition from axonal transport dynamics. *PLOS Computational Biology* **17,** e1009258.

19. Chow VW, Mattson MP, Wong PC, Gleichmann M. 2010 An overview of APP processing enzymes and products. *Neuromolecular Medicine* **12,** 1-12. (doi:10.1007/s12017-009-8104-z)

20. MacLeod R, Hillert E, Cameron RT, Baillie GS. 2015 The role and therapeutic targeting of α-, β- and γ-secretase in Alzheimer's disease. *Future Sci. OA* **1,** FSO11. (doi:10.4155/fso.15.9)

21. Morris AM, Watzky MA, Agar JN, Finke RG. 2008 Fitting neurological protein aggregation kinetic data via a 2-step, minimal/"ockham's razor" model: The finke-watzky mechanism of nucleation followed by autocatalytic surface growth. *Biochemistry* **47,** 2413-2427. (doi:10.1021/bi701899y)

22. Iashchishyn IA, Sulskis D, Nguyen Ngoc M, Smirnovas V, Morozova-Roche LA. 2017 Finke-watzky two-step nucleation-autocatalysis model of S100A9 amyloid formation: Protein misfolding as "nucleation" event. *ACS Chem. Neurosci.* **8,** 2152-2158. (doi:10.1021/acschemneuro.7b00251)

23. Thacker D, Barghouth M, Bless M, Zhang E, Linse S. 2023 Direct observation of secondary nucleation along the fibril surface of the amyloid β 42 peptide. *Proceedings of the National Academy of Sciences* **120,** e2220664120. (doi:10.1073/pnas.2220664120)

24. Bieschke J, Zhang Q, Powers ET, Lerner RA, Kelly JW. 2005 Oxidative metabolites accelerate Alzheimer's amyloidogenesis by a two-step mechanism, eliminating the requirement for nucleation. *Biochemistry* **44,** 4977-4983. (doi:10.1021/bi0501030)

25. Vestergaard M, Kerman K, Saito M, Nagatani N, Takamura Y, Tamiya E. 2005 A rapid label-free electrochemical detection and kinetic study of Alzheimer's amyloid beta aggregation. *J. Am. Chem. Soc.* **127,** 11892-11893. (doi:10.1021/ja052522q)

26. Cruz L, Urbanc B, Buldyrev SV, Christie R, Gómez-Isla T, Havlin S, McNamara M, Stanley HE, Hyman BT. 1997 Aggregation and disaggregation of senile plaques in Alzheimer disease. *Proc. Natl. Acad. Sci. U. S. A.* **94,** 7612-7616. (doi:10.1073/pnas.94.14.7612)

27. Haass C, Kaether C, Thinakaran G, Sisodia S. 2012 Trafficking and proteolytic processing of APP. *Cold Spring Harb Perspect. Med.* **2,** a006270. (doi:10.1101/cshperspect.a006270)

28. Masters CL, Selkoe DJ. 2012 Biochemistry of amyloid β-protein and amyloid deposits in Alzheimer disease. *Cold Spring Harb Perspect. Med.* **2,** a006262. (doi:10.1101/cshperspect.a006262)

29. Madrasi K, Das R, Mohmmadabdul H, Lin L, Hyman BT, Lauffenburger DA, Albers MW, Rissman RA, Burke JM, Apgar JF, Wille L, Gruenbaum L, Hua F. 2021 Systematic in silico analysis of clinically tested drugs for reducing amyloid-beta plaque accumulation in Alzheimer's disease. *Alzheimer's Dement.* **17,** 1487-1498. (doi:10.1002/alz.12312)

30. Querol-Vilaseca M, Colom-Cadena M, Pegueroles J, Nuñez-Llaves R, Luque-Cabecerans J, Muñoz-Llahuna L, Andilla J, Belbin O, Spires-Jones T, Gelpi E, Clarimon J, Loza-Alvarez P, Fortea J, Lleó A. 2019 Nanoscale structure of amyloid-β plaques in Alzheimer's disease. *Scientific Reports* **9,** 5181. (doi:10.1038/s41598-019-41443-3)

31. Raskatov JA. 2019 What is the "Relevant" amyloid β42 concentration? *ChemBioChem* **20,** 1725-1726. (doi:10.1002/cbic.201900097)

32. Waters J. 2010 The concentration of soluble extracellular amyloid-beta protein in acute brain slices from CRND8 mice. *Plos One* **5,** e15709. (doi:10.1371/journal.pone.0015709)

33. Dubnovitsky A, Sandberg A, Rahman MM, Benilova I, Lendel C, Härd T. 2013 Amyloid-β protofibrils: Size, morphology and synaptotoxicity of an engineered mimic. *PLoS One* **8,** e66101. (doi:10.1371/journal.pone.0066101)

34. Dawkins E, Derks RJE, Schifferer M, Trambauer J, Winkler E, Simons M, Paquet D, Giera M, Kamp F, Steiner H. 2023 Membrane lipid remodeling modulates γ-secretase processivity. *J. Biol. Chem.* **299,** (doi:10.1016/j.jbc.2023.103027)

35. Kuznetsov IA, Kuznetsov AV. 2022 An analytical solution simulating growth of lewy bodies. *Math. Med. Biol.* **39,** 299-312. (doi:10.1093/imammb/dqac006)

36. Meyer-Luehmann M, Spires-Jones TL, Prada C, Garcia-Alloza M, de Calignon A, Rozkalne A, Koenigsknecht-Talboo J, Holtzman DM, Bacskai BJ, Hyman BT. 2008 Rapid appearance and local toxicity of amyloid-beta plaques in a mouse model of Alzheimer's disease. *Nature* **451,** 720-724. (doi:10.1038/nature06616)

37. Yan P, Bero AW, Cirrito JR, Xiao Q, Hu X, Wang Y, Gonzales E, Holtzman DM, Lee J. 2009 Characterizing the appearance and growth of amyloid plaques in APP/PS1 mice. *J. Neurosci.* **29,** 10706-10714. (doi:10.1523/JNEUROSCI.2637-09.2009)

38. Beck JV, Arnold KJ. 1977 *Parameter Estimation in Science and Engineering.* New York: Wiley.

39. Zadeh KS, Montas HJ. 2010 A class of exact solutions for biomacromolecule diffusion-reaction in live cells. *J. Theor. Biol.* **264,** 914-933. (doi:10.1016/j.jtbi.2010.03.028)

40. Zi Z. 2011 Sensitivity analysis approaches applied to systems biology models. *IET Systems Biology* **5,** 336-346. (doi:10.1049/iet-syb.2011.0015)

41. Kuznetsov IA, Kuznetsov AV. 2019 Investigating sensitivity coefficients characterizing the response of a model of tau protein transport in an axon to model parameters. *Comput. Methods Biomech. Biomed. Engin.* **22,** 71-83. (doi:10.1080/10255842.2018.1534233)

42. Kacser H, Burns JA, Fell DA. 1995 The control of flux. *Biochem. Soc. Trans.* **23,** 341-366. (doi:10.1042/bst0230341)

43. Saido T, Leissring MA. 2012 Proteolytic degradation of amyloid β-protein. *Cold Spring Harb Perspect. Med.* **2,** a006379. (doi:10.1101/cshperspect.a006379)

44. Kuznetsov AV. 2023 Effect of diffusivity of amyloid beta monomers on the formation of senile plaques. *bioRxiv* 2023.07.31.551367. (doi:10.1101/2023.07.31.551367)

Figure captions

Fig. 1. A cubic CV with a side length of L containing a single growing Aβ plaque.

Fig. 2. (a) Molar concentration of Aβ aggregates, C_B, over time (in years). (b) Similar to Fig. 2a, but focusing on a specific time range of [0 1 year] on the *x*-axis. The numerical solution is obtained by solving Eqs. (3) and (4) numerically with the initial condition (5). The approximate solution is plotted using Eq. (16) and converting the dimensionless variables into dimensional ones. The approximate solution is valid only for $T_{1/2,A} \to \infty$ and is plotted exclusively for this case.

Fig. 3. (a) Molar concentration of Aβ monomers, C_A, over time (in years). (b) Similar to Fig. 3a, but zooming in on a specific time range of [0 1 year] on the *x*-axis. The numerical solution is obtained by numerically solving Eqs. (3) and (4) with the initial condition (5). The approximate solution is plotted using Eqs. (15) and converting the dimensionless variables into dimensional ones. The approximate solution is valid only for $T_{1/2,A} \to \infty$ and is plotted exclusively for this case.

Fig. 4. Radius of a growing Aβ plaque, r_{ABP}, over time (in years). (b) Similar to Fig. 4a, but focusing on a specific time range of [0 1 year] on the *x*-axis. The numerical solution is obtained by numerically solving Eqs. (3) and (4) with the initial condition (5) and then using Eq. (19) to calculate the radius of the Aβ plaque. The dimensionless variables are then converted into dimensional ones. The approximate solution is plotted using Eq. (21). The approximate solution is valid only for $T_{1/2,A} \to \infty$ and is plotted exclusively for this case.

Fig. 5. Radius of a growing Aβ plaque after 20 years of growth vs (a) half distance between senile plaques, (b) rate of production of Aβ monomers, and (c) average volume of an Aβ fibril composing an Aβ plaque.

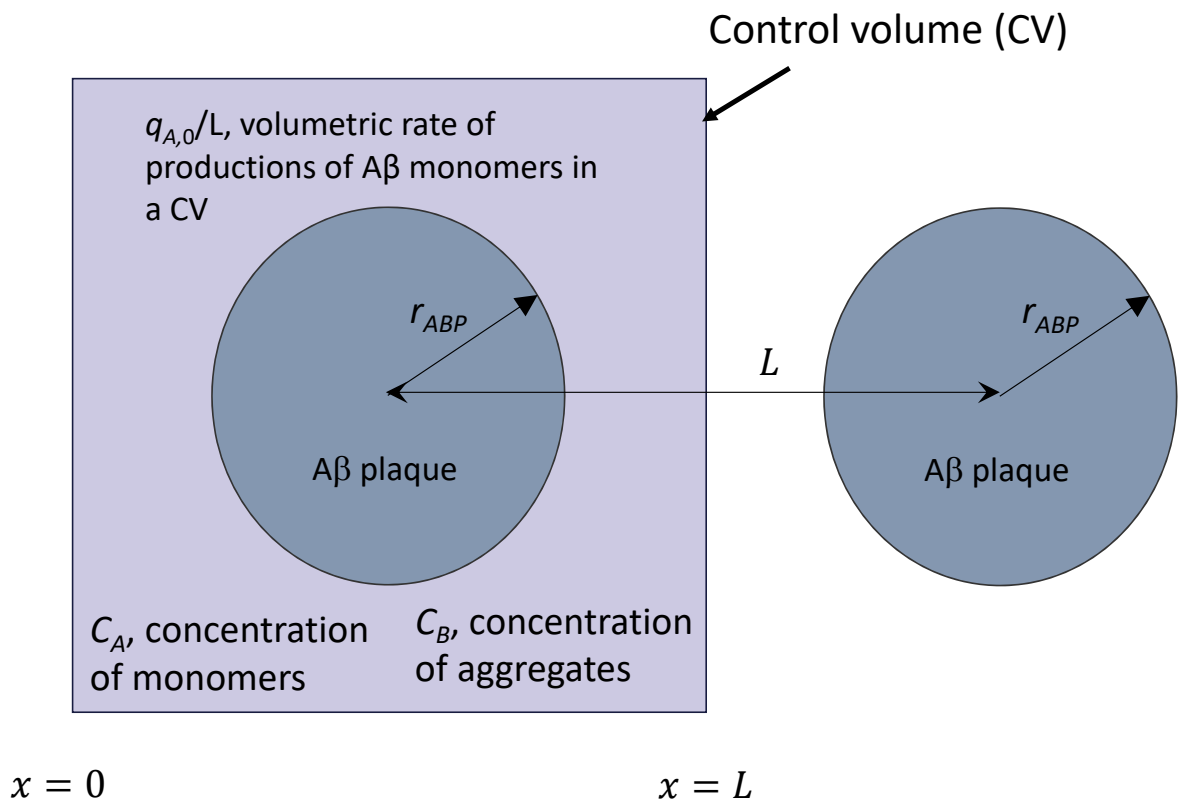
Control volume (CV)
$q_{A,0}$/L, volumetric rate of productions of Aβ monomers in a CV
r_{ABP}
L
r_{ABP}
Aβ plaque
Aβ plaque
C_A, concentration of monomers
C_B, concentration of aggregates
$x = 0$
$x = L$

Figure 1

(a)

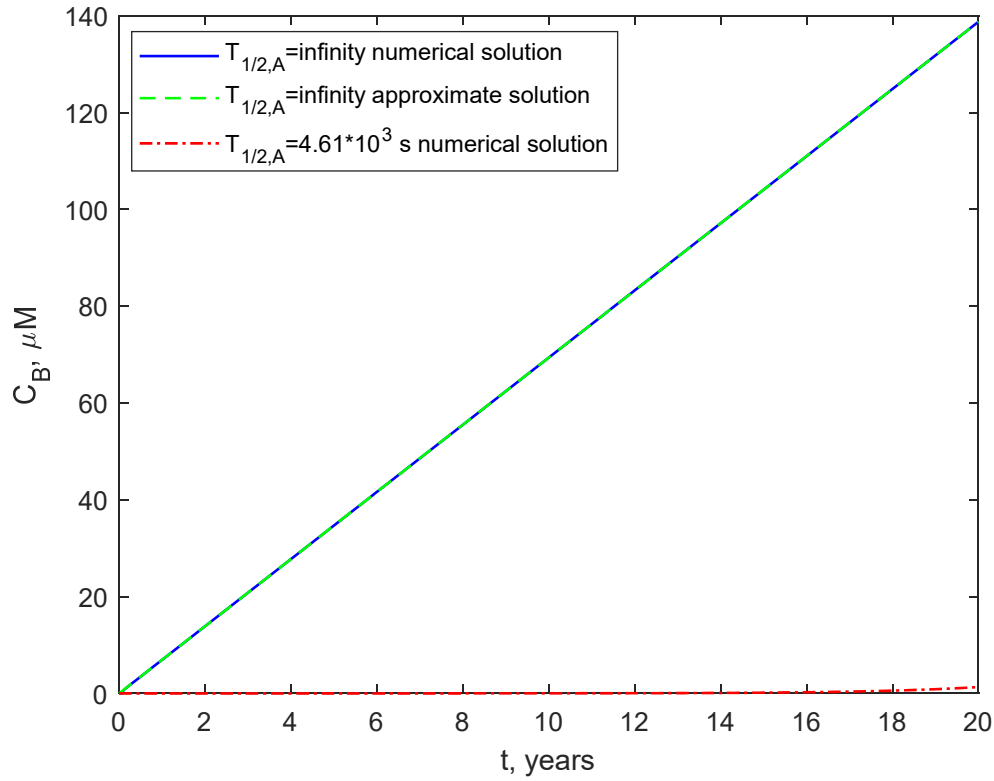

(b)

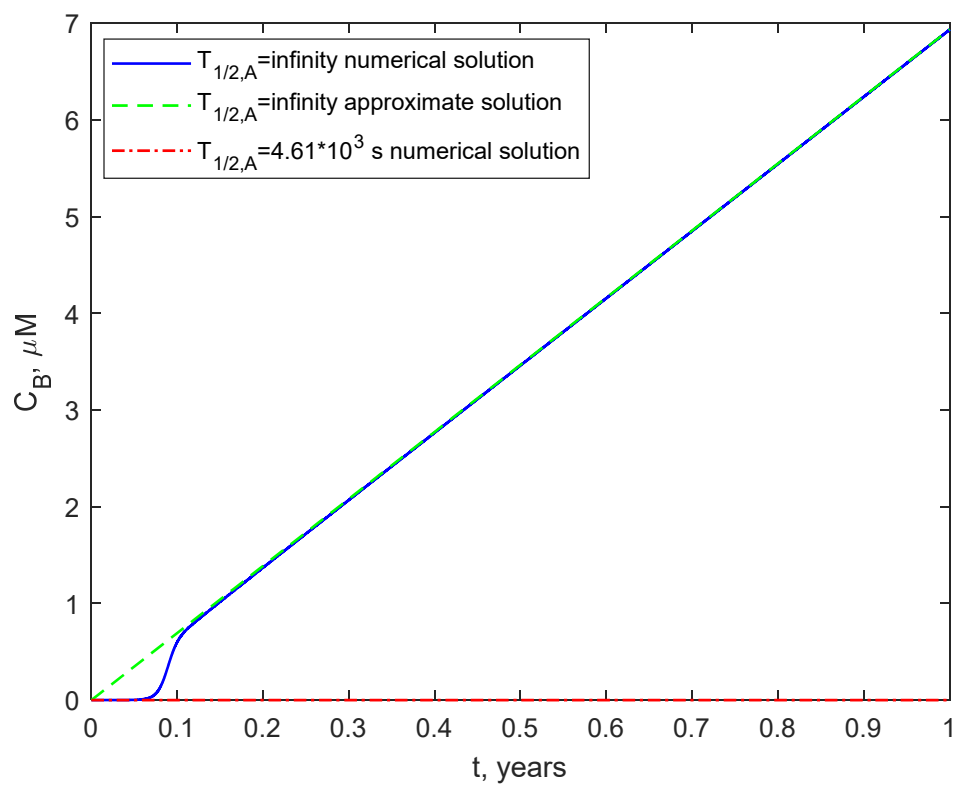

Figure 2a,b

(a)

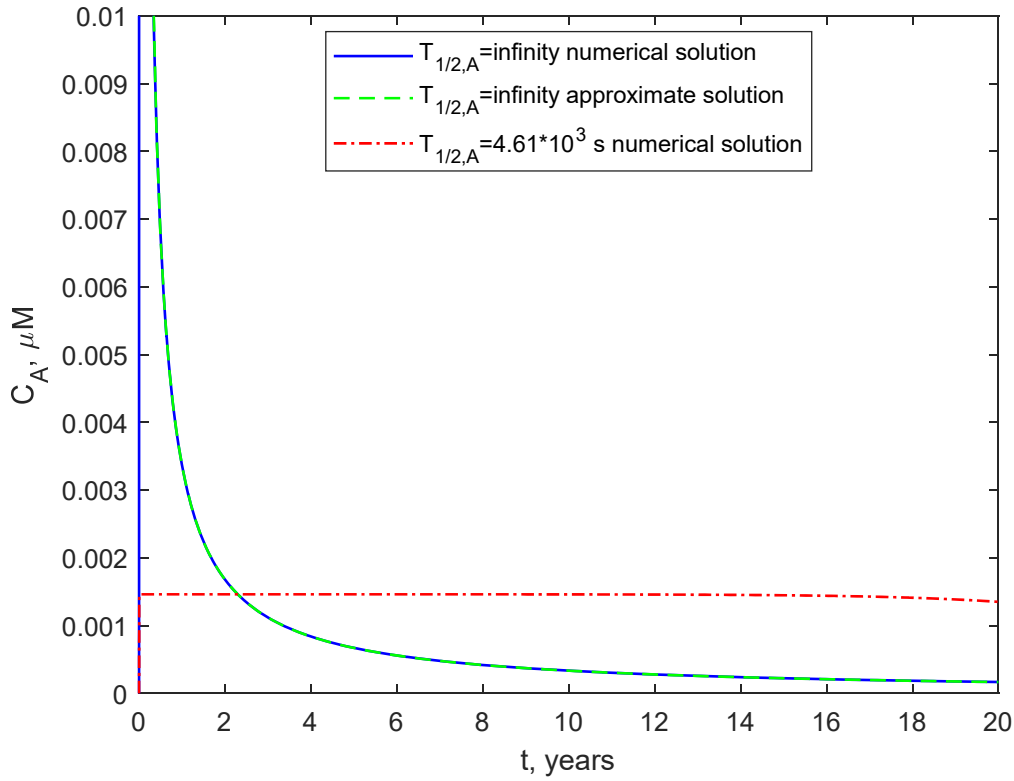

(b)

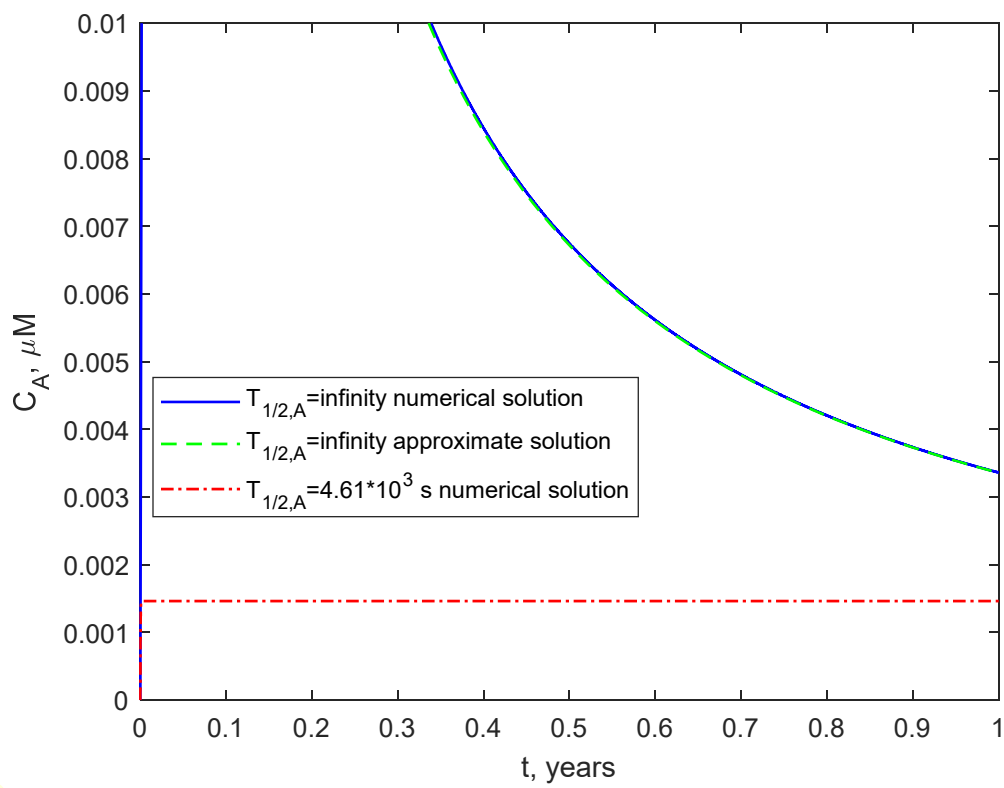

Figure 3a,b

(a)

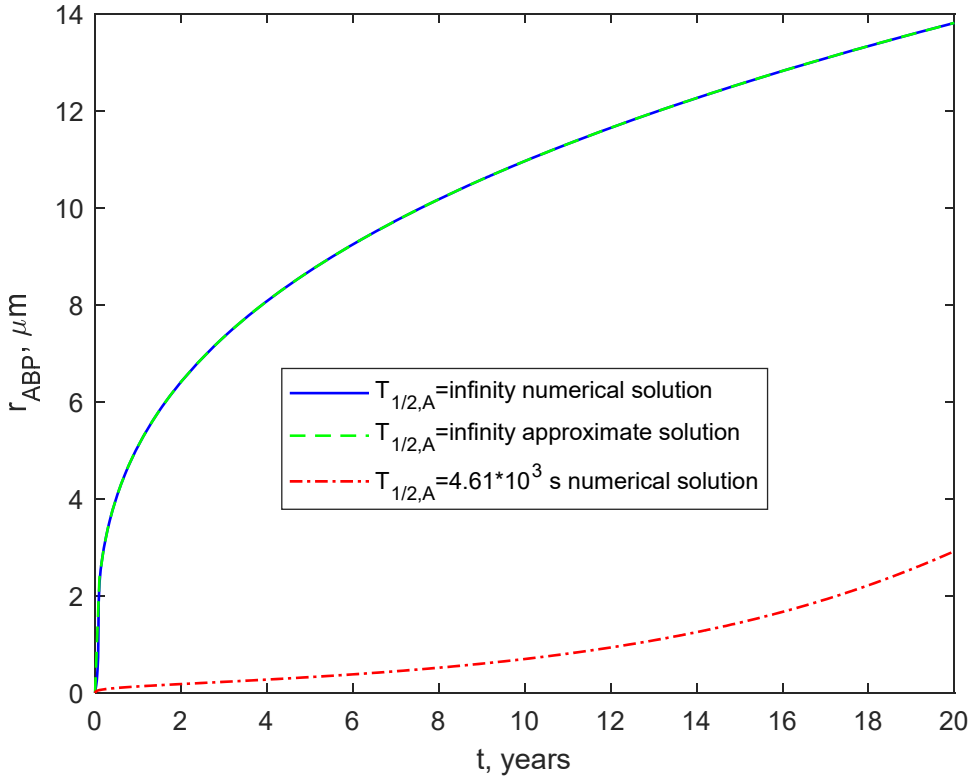

(b)

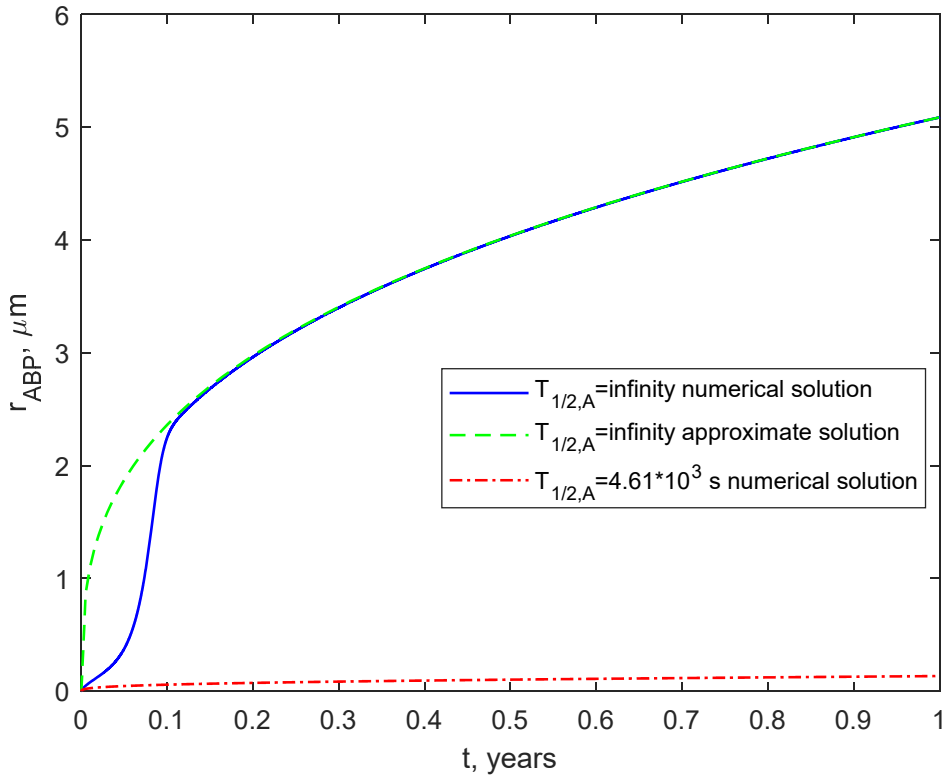

Figure 4a,b

(a)

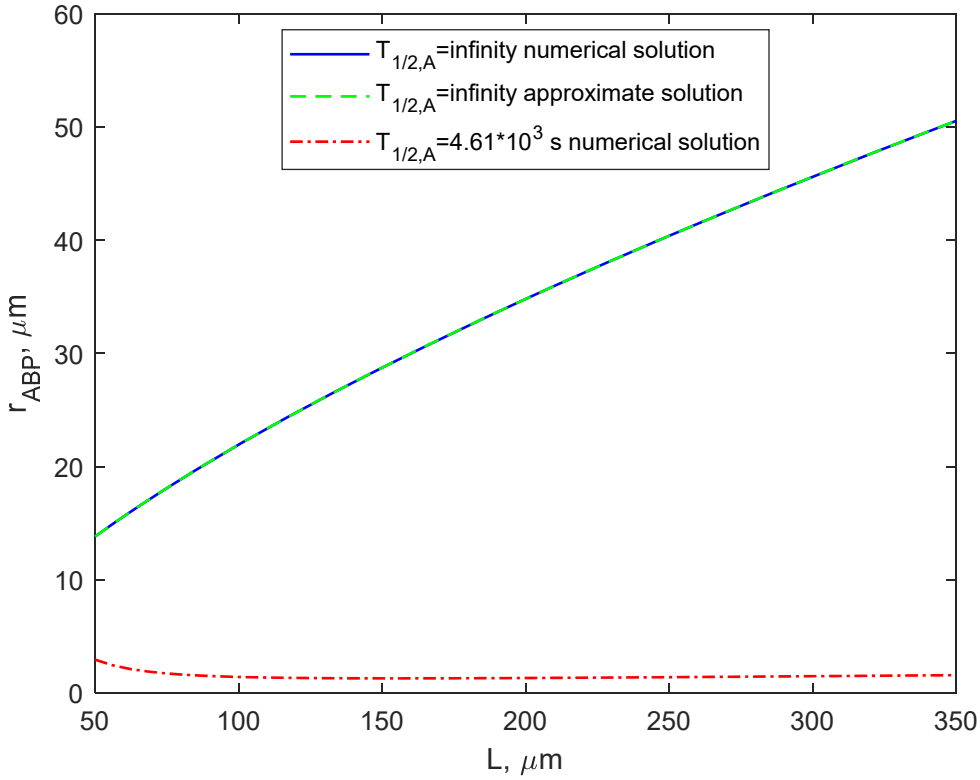

(b)

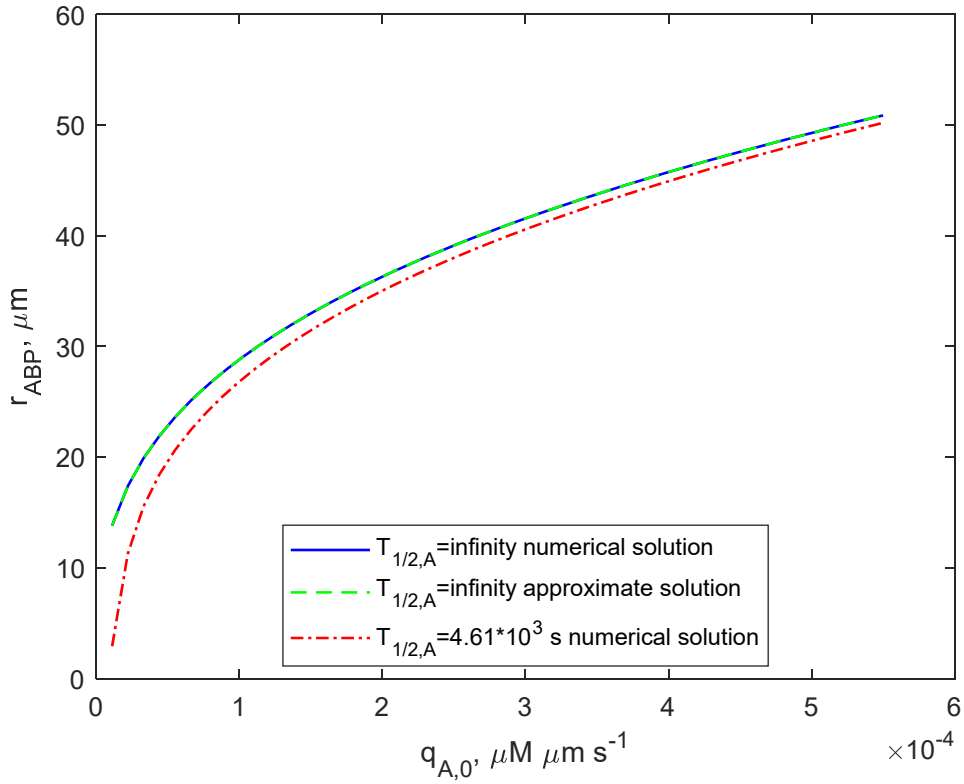

Figure 5a,b

(c)

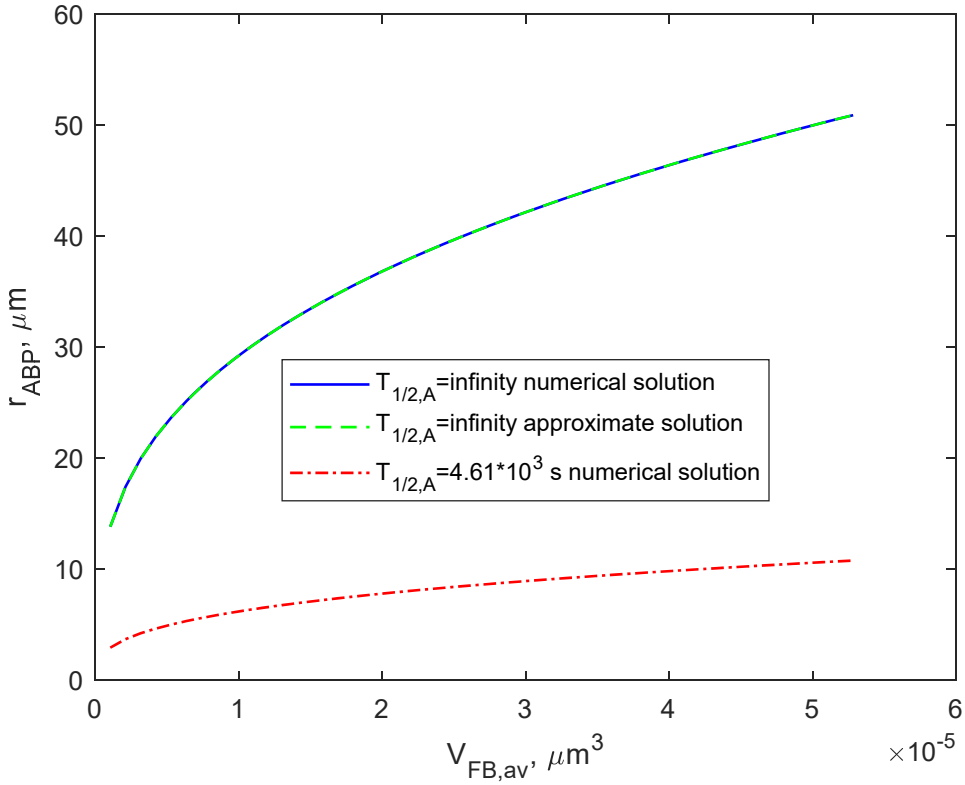
60
50
40
30
20
10
0
0
1
2
3
4
5
6
r_{ABP}, μm
$V_{FB,av}$, μm^3
$\times 10^{-5}$
$T_{1/2,A}$=infinity numerical solution
$T_{1/2,A}$=infinity approximate solution
$T_{1/2,A}$=4.61*10^3 s numerical solution

Figure 5c